

# Prediction of aerosol deposition in 90° bends using LES and an efficient Lagrangian tracking method

M. Breuer<sup>a,\*</sup>, H.T. Baytekin<sup>a</sup>, E.A. Matida<sup>b</sup>

<sup>a</sup>*Institute of Fluid Mechanics, University of Erlangen-Nürnberg, D-91058 Erlangen, Germany*

<sup>b</sup>*Department of Mechanical and Aerospace Engineering, Carleton University, Ottawa, Ont., Canada, K1S 5B6*

Received 22 November 2005; received in revised form 26 January 2006; accepted 27 January 2006

---

## Abstract

Aiming at the better prediction of pharmaceutical aerosol deposition in extrathoracic airways, a simpler test case, namely a 90° bend flow (tubular cross-section) laden with monodisperse particles, is adopted here and studied numerically. The continuous phase is calculated using a large-eddy simulation technique along with a finite-volume method for block-structured curvilinear grids. The particulate phase is simulated using a Lagrangian approach where hundred thousands of individual monodisperse particles with varying particle diameters are released and tracked throughout the computational domain. To allow such a large number of particles, a highly efficient tracking algorithm is applied, where particle paths are predicted in an orthogonal computational domain, avoiding time-consuming search algorithm, normally required when particles are tracked in the actual physical domain of a curvilinear body-fitted block-structured grid. Both simulation algorithms, for the continuous and particulate phases, are completely parallelized using domain decomposition. Additionally, the in-house code applied supports vector processing allowing efficient usage of nearly all kinds of high-performance architectures. Two different Reynolds numbers  $Re_D$  are considered where  $Re_D$  is based on the bend diameter and mean flow velocity. The first case is within the laminar regime at  $Re_D = 1000$  and serves for the purpose of verification and validation. The second, more challenging case comprises the turbulent regime at  $Re_D = 10,000$ , which is the intrinsic objective of the present study. Depending on the Stokes number of the particles,  $0.001 \leq St \leq 1.5$ , and the releasing locations at the entrance of the bend, the particles will either deposit on the wall or penetrate and exit the computational domain. Simulation results of aerosol deposition efficiency, over the entire range of particle diameters considered here, show an excellent agreement when compared to experimental values obtained by Pui, Romay-Novas, and Liu [(1987). Experimental study of particle deposition in bends of circular cross-section. *Aerosol Science and Technology*, 7, 301].

© 2006 Elsevier Ltd. All rights reserved.

**Keywords:** Monodisperse aerosols; Particle deposition; Large-eddy simulation; Eulerian-Lagrangian approach; Efficient tracking algorithm

---

\* Corresponding author. Tel.: +49 9131 852 9509; fax: +49 9131 852 9579.

E-mail address: [breuer@lstm.uni-erlangen.de](mailto:breuer@lstm.uni-erlangen.de) (M. Breuer).

## Nomenclature

$A$	area
$A^+$	constant in wall damping function
$C$	Cunningham slip correction factor
$C_D$	drag coefficient
$C_s$	Smagorinsky constant
$d$	diameter
$D$	diameter of the bend
$De$	Dean number ( $=Re_D/\sqrt{R_0}$ )
$\mathbf{F}$	forces (vector)
$\mathbf{g}$	gravitational acceleration vector
$I_c$	interception parameter ( $=d_p/D$ )
$k$	turbulent kinetic energy
$l$	subgrid length
$N$	number of particles
$p, P$	pressure
$P$	penetration ratio ( $=1 - \eta$ ) (%)
$r$	radius
$R_0$	curvature ratio ( $=R_b/(D/2)$ )
$R_b$	axial radius of curvature of the bend
$Re_D$	flow Reynolds number based on diameter ( $=U_m D/v_f$ )
$Re_p$	particle Reynolds number ( $= \mathbf{u}_f - \mathbf{u}_p  d_p/v_f$ )
$Re_p^*$	particle Reynolds number ( $=U_m d_p/v_f$ )
$S_{ij}$	strain rate tensor
$St$	Stokes number ( $=C \rho_p d_p^2 U_m / (18 \mu_f D / 2)$ )
$t, T$	time
$u_i$	Cartesian velocity components
$\mathbf{u} = (u, v, w) = u_i$	velocity vector
$u_\tau$	friction velocity
$\mathbf{U} = (U, V, W)$	contravariant velocity
$U_m$	mean axial fluid velocity
$V$	volume
$(x, y, z) = x_i$	Cartesian coordinate system directions
$y^+$	dimensionless distance from the wall
<i>Greek letters</i>	
$\alpha$	drag correction factor
$\varepsilon$	dissipation rate of turbulent kinetic energy
$\delta_{ij}$	Kronecker delta
$\Delta$	filter width
$\Delta n_p$	normal distance of the particle center to the surface
$\Delta t$	time step size
$\Delta x, \Delta y, \Delta z$	grid spacing
$\omega$	specific dissipation rate
$\rho$	density
$\mu$	dynamic viscosity
$\nu$	kinematic viscosity
$\xi, \eta, \zeta$	coordinates in $c$ -space
$\eta$	deposition efficiency ( $=N_{\text{deposited}}/N_{\text{total}}$ ) (%)
$\tau_p$	particle relaxation time
$\tau_w$	wall shear stress
$\tau_{ij}$	stress tensor

***Subscripts***

B	buoyancy
D	drag
f	fluid
G	gravity
$i, j, k$	indices
p	particle
T	turbulent
w	wall

***Superscripts***

( $\cdot$ )	filtered quantity
a	anisotropic
$i, j, k$	indices
SGS	subgrid scale
mol	molecular

## 1. Introduction

Aerosol drug delivery (Finlay, 2001) into the lungs through the oral cavity has become an established method in the treatment of lung disease and has a great potential for other non-lung diseases. The drug is normally generated in form of solid or liquid particles from devices such as nebulizers, pressurized metered dose inhalers (pMDIs) or dry powder inhalers (DPIs). Although the lung is the target, part of the dose is typically lost through deposition on the walls of the extrathoracic region (from the mouth opening to the end of the trachea). That leads to deviations from the ideal delivery and unwanted side effects. Consequently, the deposition in the mouth–throat region itself has become an important issue.

To study aerosol deposition, a variety of in vitro measurements in idealized mouth–throat models have been carried out. The most important factors determining the deposition were identified and summarized by Finlay (2001): the geometry of the airway of the patient, the inhaled mass flow rate, the characteristic properties of the particles, and the inhalation device (see, e.g., DeHaan & Finlay, 2001). A variety of experimental as well as numerical investigations were carried out. Stahlhofen, Rudolf, and James (1989) provided a detailed review on all experimental deposition studies carried out in human subjects.

In order to gain a better physical understanding of the aerosol deposition, numerical simulations are extremely useful. A few should be mentioned here. For example, Stapleton, Guentsch, Hoskinson, and Finlay (2000) investigated the aerosol deposition in the mouth–throat region using the Reynolds–Averaged Navier–Stokes equations (RANS) combined with a standard  $k-\varepsilon$  turbulence model. They found out that such two-equation models perform poorly for the flow in the mouth–throat geometry. The reason for this behavior is well-known; the flow problem considered shows many complex flow phenomena such as curved streamlines and secondary flow regions for which isotropic, zero-, one- or two-equation eddy–viscosity models developed for simple flows of boundary-layer type are not well suited. Furthermore, the present flow is in a range of Reynolds numbers where transitional effects may occur, whereas standard  $k-\varepsilon$  or  $k-\omega$  models are appropriate for high Reynolds number flows only. Hence, the prediction of particle deposition using a Lagrangian method to track the particles in the flow field is highly inaccurate if the continuous phase is not predicted reliably.

Matida, Finlay, Lange, and Grgic (2004) investigated the deposition of monodisperse particles in an idealized geometry based on a standard  $k-\omega$  model for the continuous phase and a Lagrangian random-walk eddy-interaction model (EIM) for the particulate phase. The RANS/EIM results clearly indicate that the model is not capturing relevant features of the flow. Compared with the experimental fitting curve of Stahlhofen et al. (1989), the total deposition rate is highly overpredicted over the entire range of particle diameters. Furthermore, the so-called “mean flow tracking”, where no turbulent particle dispersion is taken into account, shows a poor agreement with experimental measurements

too. An additional prediction of the deposition rates applying a standard  $k-\varepsilon$  model leads to even larger deviations than the  $k-\omega$  model. Only with a special near-wall correction in the EIM, which takes the anisotropy of the Reynolds stresses in the vicinity of walls into account, improved results of the deposition rates could be achieved. However, the remaining discrepancies found between the calculations and the experiments are still of the order of 15–25%.

[McFarland, Gong, Muyshondt, Wente, and Anand \(1997\)](#) tried to overcome the shortcomings of two-equation models by applying a Reynolds stress model to describe the turbulent behavior of bend flows. The particle motion was predicted in a Lagrangian frame of reference with a random walk model to describe turbulent fluctuations. A variety of numerical investigations were carried out to determine the most important influencing factors on particle deposition, e.g., turbulence level,  $Re$  number,  $St$  number, curvature ratio. Based on that they set up a correlation model for the usage by designers of aerosol transport systems in order to predict aerosol penetration. From the viewpoint of evaluating the accuracy of this correlation model, the comparison with the experimental data of [Pui, Romay-Novas, and Liu \(1987\)](#) is most striking. Although a second-moment closure was applied in the study of [McFarland et al. \(1997\)](#), the discrepancies observed for the deposition rates are of the same order of inaccuracy as for the first-moment turbulence model with near-wall correction used by [Matida et al. \(2004\)](#), e.g. a deposition rate of 37% instead of 58% found by [Pui et al. \(1987\)](#) (deviation: 21%) for a Stokes number of  $St = 0.4$ .

Consequently, the second-moment closures based on Reynolds stress models have also reliability limitations when aerosol deposition prediction in idealized or real mouth–throat geometries is concerned. Therefore, in the present study the continuous phase is simulated based on a methodology which is much more appropriate for turbulent flows including complex flow phenomena, i.e., the large-eddy simulation (LES) technique combined with a Lagrangian particle tracking algorithm for the disperse phase.

For flows in simple geometries, investigations using the same methodology are available in the literature. For example, [Chen and McLaughlin \(1995\)](#), [Uijttewaal and Oliemans \(1996\)](#), [Wang and Squires \(1996\)](#), and [Wang, Squires, Chen, and McLaughlin \(1997\)](#) studied the particle dispersion and deposition in vertical pipe and duct flows using either direct numerical simulation (DNS) or LES. Interesting results were obtained such as the different deposition behavior of small and large particles. The deposition of large particles was found to be rather insensitive to the near-wall turbulence. Owing to their large inertia, they can penetrate the viscous sublayer and impinge on the wall by the free-flight mechanism. In contrast, owing to low inertia the deposition of small particles was observed to be limited by their ability to cross the relatively quiescent near-wall layer ([Uijttewaal & Oliemans, 1996](#)) leading to the near-wall build-up of these particles.

Regarding particle-laden flows in human airways, first highly encouraging results using the Eulerian–Lagrangian method based on LES were achieved by [Matida, Breuer, Finlay, and Lange \(2004\)](#) for the deposition of monodisperse particles in a idealized mouth geometry with a small inlet diameter. Using this enhanced methodology a considerable improvement over the standard RANS/EIM approach was found which motivated further detailed investigations on this topic taking some fundamental test cases into account.

[Cheng, Zhou, and Chen \(1999\)](#) suggested that the deposition in curved pipes could be used to model the oral deposition. This basic flow problem of inertial deposition of aerosol particles in bends also plays a major role in many practical applications such as aerosol sampling and transport systems. Experimentally, it was investigated for a wide range of curvature ratios (ratio of bend curvature radius at the centerline to the tube radius) and Reynolds numbers, see, e.g., [McFarland et al. \(1997\)](#) and [Pui et al. \(1987\)](#). Summarizing the outcome of these studies, the curvature ratio only weakly affects the deposition rate. Furthermore, the flow Reynolds number also has a mild effect on the deposition efficiency. For the turbulent case in the range  $6000 \leq Re_D = U_m D/v_f \leq 10,000$ , [Pui et al. \(1987\)](#) found no dependence on the flow Reynolds number.

As a first step towards the entire geometry of the extrathoracic region, in the present investigation, a simpler test case is considered where the geometry and flow parameters rely on the 90° bend experiment of [Pui et al. \(1987\)](#). Here, the deposition efficiency of liquid monodisperse particles in tube bends with a circular cross-section was measured for different flow ( $Re_D$ ) and particle Reynolds numbers ( $Re_p$ ). The curvature ratio of the bend is 5.6–5.7 and hence the flow is in the large Dean number range ( $De = 4225$ ). The particles adhere to the tube surface upon contact and particle bounce from the bend is not considered in the current study.

The paper is organized as follows. The next section provides a description of the numerical methodology separated into the large-eddy simulation technique for the continuous phase and the Lagrangian tracking algorithm for the particulate phase. Special emphasis is put on an efficient tracking algorithm. In Section 3 the test case of the curved bend flow is described in detail. Finally, Section 4 discusses the results obtained including a comparison with experimental reference data.

## 2. Numerical methodology

### 2.1. Continuous phase

An inherent property of the Navier–Stokes equations is their capability to describe even the most complex turbulent flow. It is well known that in principle no turbulence modeling is necessary. However, DNS is totally impractical for high Reynolds number flows. Statistical turbulence models based on the Reynolds-averaged equations have been developed for decades with limited success, especially for highly complex turbulent flows as described in the Introduction. This is due to the fact that these approaches have to describe the whole spectrum of turbulent eddies. The concept of LES overcomes this drawback. Only the influence of the small eddies (supposed to be more universal, random, homogeneous and isotropic) has to be modeled by a subgrid-scale model whereas the large energy-carrying eddies are computed directly.

#### 2.1.1. Governing equations

In order to separate the large- and small-scale motions, the 3D, time-dependent Navier–Stokes equations are filtered. Here, a box filter with the filter width  $\Delta$  is applied as a filter kernel and an incompressible fluid is assumed. The governing equations read in their dimensionless form

$$\frac{\partial \bar{u}_j}{\partial x_j} = 0, \quad (1)$$

$$\frac{\partial \bar{u}_i}{\partial t} + \frac{\partial (\bar{u}_i \bar{u}_j)}{\partial x_j} = -\frac{\partial \bar{p}}{\partial x_i} - \frac{1}{Re_D} \frac{\partial \tau_{ij}^{\text{mol}}}{\partial x_j} - \frac{\partial \tau_{ij}^{\text{SGS}}}{\partial x_j}, \quad (2)$$

$$\tau_{ij}^{\text{mol}} = -2v\bar{S}_{ij} \quad \text{where } \bar{S}_{ij} = \frac{1}{2} \left( \frac{\partial \bar{u}_i}{\partial x_j} + \frac{\partial \bar{u}_j}{\partial x_i} \right), \quad (3)$$

where  $u_i$ ,  $p$  and  $v = \mu$  ( $\rho = 1$ ) are the velocity component, the pressure and the viscosity, respectively. The overbar ( $\cdot$ ) defines the resolved scales.  $Re_D$  is the characteristic flow Reynolds number defined below. The term  $\tau_{ij}^{\text{mol}}$  describes the momentum transport due to molecular motion, which for a Newtonian fluid is given by Eq. (3). Owing to filtering of the non-linear convective term in the momentum equation (2), the additional subgrid-scale (SGS) stress tensor  $\tau_{ij}^{\text{SGS}}$  arises which has to mimic the influence of the non-resolved small-scale structures on the resolved large eddies. Only this effect has to be modeled by a subgrid scale model. For simplicity, the mass and momentum conservation equations (1) and (2) are given here in Cartesian coordinates. However, the computation of flows in complex geometries requires curvilinear boundary-fitted (block-structured) grids which in general are non-orthogonal. By applying a coordinate transformation, the governing equations can easily be rewritten for a general system of coordinates as used in the computer code.

#### 2.1.2. Subgrid-scale modeling

In principle, the LES concept leads to a closure problem similar to that obtained by RANS. However, the non-resolvable small scales in an LES are much less problem-dependent than the large scale motion so that the subgrid-scale turbulence can be represented by relatively simple models, e.g., zero-equation eddy–viscosity models. Like other eddy–viscosity models the well known and most often used Smagorinsky model (Smagorinsky, 1963) is based on Boussinesq's approximation which describes the stress tensor  $\tau_{ij}^{\text{SGS}}$  as the product of the strain rate tensor  $\bar{S}_{ij}$  and an eddy viscosity  $v_T$ :

$$\tau_{ij}^{\text{SGS},a} = \tau_{ij}^{\text{SGS}} - \delta_{ij}\tau_{kk}^{\text{SGS}}/3 = -2v_T\bar{S}_{ij}, \quad (4)$$

where  $\tau_{ij}^{\text{SGS},a}$  is the anisotropic (traceless) part of the stress tensor  $\tau_{ij}^{\text{SGS}}$  and  $\delta_{ij}$  is the Kronecker delta. The trace of the stress tensor is added to the pressure resulting in the new pressure  $P = \bar{p} + \tau_{kk}^{\text{SGS}}/3$ . The eddy viscosity  $v_T$  itself is a

function of the strain rate tensor  $\bar{S}_{ij}$  and the subgrid length  $l$ , as

$$v_T = l^2 |\bar{S}_{ij}| \quad \text{with} \quad l = C_s \Delta \left[ 1 - \exp \left( \frac{-y^+}{A^+} \right)^3 \right]^{0.5},$$

$$\Delta = (\Delta x \cdot \Delta y \cdot \Delta z)^{1/3}, \quad y^+ = \frac{yu_\tau}{v}, \quad u_\tau = \sqrt{\frac{\tau_w}{\rho}} \quad \text{and} \quad A^+ = 25. \quad (5)$$

$C_s$  is the well-known Smagorinsky constant which has to be prescribed as a fixed value in the entire integration domain or can be determined as a function of time and space by the dynamic procedure originally proposed by Germano, Piomelli, Moin, and Cabot (1991) and later improved by several authors, e.g. Lilly (1992). In the first case, a Van Driest damping function is required (see Eq. (5)) in order to take the reduction of the subgrid length  $l$  near solid walls into account. In the present investigation, the fixed parameter version of the Smagorinsky model was applied. A theoretical value for the Smagorinsky constant ( $C_s = 0.165$ ) can be derived for homogeneous isotropic flows (Lilly, 1967). For practically relevant inhomogeneous and anisotropic shear flows, however, smaller values of  $C_s$  were found to be more appropriate. Therefore, the present simulations were carried out with the well established standard constant  $C_s = 0.1$ . Since the influence of the SGS model is expected to be small due to the low Reynolds number of this investigation (see, e.g., Breuer, 1998, 2002), the dynamic version of the model was not considered.

### 2.1.3. Finite-volume method

The computer code *LESOC* (=Large-Eddy Simulation On Curvilinear Coordinates, Breuer, 1998, 2000, 2002; Breuer & Rodi, 1996) is used for integrating the governing equations in space and time. It is based on a 3D finite-volume method for arbitrary non-orthogonal and block-structured grids. All viscous fluxes are approximated by central differences of second-order accuracy, which fits the elliptic nature of the viscous effects. As shown in Breuer (1998, 2002), the quality of LES predictions is strongly dependent on low-diffusive discretization schemes for the non-linear convective fluxes in the momentum equation (2). Although several schemes are implemented in the code applied, the central scheme of second-order accuracy (CDS-2) is preferred for the LES predictions in the present work.

Time advancement is performed by a predictor–corrector scheme. A low-storage multi-stage Runge–Kutta method (three sub-steps, second-order accuracy) is applied for integrating the momentum equations in the predictor step. Within the corrector step, the Poisson equation for the pressure correction is solved implicitly by the incomplete LU decomposition method of Stone (1968). Explicit time marching works well for LES with small time steps which are necessary to resolve turbulence motion in time. The pressure and velocity fields on a non-staggered grid are coupled by the momentum interpolation technique of Rhie and Chow (1983). A variety of different test cases (see, e.g., Breuer, 1998, 2000, 2002; Breuer & Rodi, 1996) served for the purpose of the code validation.

The algorithm is highly vectorized and additionally parallelized by domain decomposition with explicit message-passing based on message passing interface (MPI) allowing efficient computations especially on vector-parallel machines and symmetric multi-processing (SMP) clusters. The present simulations were carried out on a SGI Altix cluster applying five processors.

## 2.2. Particulate phase

### 2.2.1. Governing equations

In the present study the particle-laden flow is predicted by an Eulerian–Lagrangian approach. The continuous phase is determined by the filtered Navier–Stokes equations in the Eulerian frame of reference using LES (see Section 2.1). The dispersed phase is simulated in a Lagrangian frame of reference by simultaneously tracking a large number of single particles through the continuous flow field. Thus, the corresponding governing equations for the prediction of the particle motion do not rely on the continuum assumption.

The volume fraction of the particles in the present application are usually in the order of  $10^{-6}$  or less. The mean distance between the particles is assumed to be at least one order of magnitude larger than the diameter of the particles. Thus, a one-way coupling is taken into account where the particle motion is treated as having no effect on the fluid motion. Additionally, particle–particle interactions can be ignored.

The dispersed phase is computed based on Newton's second law taking only drag, gravity and buoyancy into account:

$$\rho_p V_p \frac{d\mathbf{u}_p}{dt} = \mathbf{F}_D + \mathbf{F}_G + \mathbf{F}_B, \quad (6)$$

where  $\rho_p$  denotes the particle density,  $V_p$  the particle volume and  $\mathbf{u}_p$  the particle velocity. Owing to the high density ratio of the uniform droplets ( $\rho_p/\rho_f = 755 \gg 1$ ;  $\rho_f$  = density of the fluid) all other contributions (e.g., added-mass force and forces due to the fluid pressure gradient and viscous stresses) can be neglected. If required for other applications, these additional forces can easily be included in the algorithm.

The particles are assumed to be rigid and spherical. Then the forces in Eq. (6) can be determined leading to the governing equation of particle motion

$$\frac{d\mathbf{u}_p}{dt} = \frac{\mathbf{u}_p - \bar{\mathbf{u}}_f}{\tau_p/\alpha} - \mathbf{g} \left( 1 - \frac{\rho_f}{\rho_p} \right), \quad (7)$$

where  $\mathbf{u}_f$  is the fluid velocity at the position of the particle and  $\mathbf{g}$  is the gravitational acceleration vector. Presently, the filtered velocity  $\bar{\mathbf{u}}_f$  is used as the corresponding fluid velocity  $\mathbf{u}_f$ . In principle, it is also possible to add a subgrid-scale contribution to the filtered quantity which is important for high- $Re$  flows. In the present applications involving moderate Reynolds numbers and a fine (nearly DNS-like) resolution of the flow field (see Section 3.3), the subgrid-scale contribution to the turbulent kinetic energy is small and hence this procedure was found to be not necessary, especially for the high density ratio  $\rho_p/\rho_f$  considered in the present study (cf. Armenio, Piomelli, & Fiorotto, 1999; Wang & Squires, 1996).

The drag force on the particle is based on Stokes flow around a sphere where the corresponding drag coefficient is given by

$$C_D = \frac{24}{Re_p} \alpha \quad \text{with} \quad Re_p = \frac{|\mathbf{u}_f - \mathbf{u}_p| d_p}{\nu_f}. \quad (8)$$

Here,  $d_p$  denotes the particle diameter,  $\nu_f = \mu_f/\rho_f$  the kinematic viscosity of the fluid and  $Re_p$  the particle Reynolds number, respectively. In order to extent the validity of relation (8) towards higher particle Reynolds number ( $0 < Re_p \leq 800$ ), the correction factor  $\alpha = 1 + 0.15 Re_p^{0.687}$  is introduced (Schiller & Naumann, 1933). Finally, the particle relaxation time in Eq. (7) is defined as

$$\tau_p = \frac{C \rho_p d_p^2}{18 \mu_f}. \quad (9)$$

It describes the response time of a particle to changes in the flow field, i.e., tiny particles possess a very short relaxation time so that they follow the continuous flow more or less without delay, whereas owing to inertia large particles need a certain time to adjust themselves to changes in the flow field. For extremely small particle sizes in the slip regime ( $d_p \lesssim 1 \mu\text{m}$ ) the Cunningham slip correction factor  $C \geq 1$  has to be taken into account. Since the range of interesting particle diameters for aerosol deposition is beyond that limit,  $C$  is presently set to unity. Integrating Eq. (7) leads to the particle velocity  $\mathbf{u}_p$ . Using the definition of the particle velocity,

$$\frac{d\mathbf{x}_p}{dt} = \mathbf{u}_p, \quad (10)$$

the actual position of the particle can be determined by a second integration.

### 2.2.2. First numerical integration

The ordinary differential equation (7) for the particle motion is integrated by a fourth-order Runge–Kutta scheme which is stable under the condition  $0 \leq \beta = \Delta t \alpha/\tau_p \leq 2.78$ . In principle, different time step sizes  $\Delta t$  can be applied for the continuous phase and the particulate phase. However, typical time step sizes used for LES are of the order of  $CFL = \mathcal{O}(1)$  (Courant–Friedrichs–Levy) and should therefore be also appropriate for tracking particles. Hence, additional implementation and run-time overheads for an interpolation procedure between time steps required for different time step sizes should be circumvented. To avoid the violation of the stability condition occurring for tiny particles with  $\tau_p$  tending towards zero, an analytical integration is used if  $\beta$  is out of the stability bounds.

### 2.2.3. Interpolation scheme

In order to integrate Eq. (7), the local instantaneous flow velocities  $\mathbf{u}_f$  predicted by LES are required at the position of the particle. If the exact position of the particle is known, the fluid velocity  $\mathbf{u}_f$  is interpolated trilinearly to the location of the particle based on the eight surrounding nodes of the grid. This interpolation is done in the so-called computational space or in short *c-space* ( $\xi, \eta, \zeta$ ) and not in the physical space abbreviated by *p-space* ( $x, y, z$ ). The reason and the advantages for this procedure will become clear when the tracking algorithm is discussed. In *c-space*, the grid spacing is equidistant, i.e.,  $\Delta\xi = \Delta\eta = \Delta\zeta = 1$  and the grid is orthogonal. Hence, the interpolation formula for the fluid velocity at the particle position  $\mathbf{u}_f|_{\text{particle}}$  is given by

$$\begin{aligned}\mathbf{u}_f|_{\text{particle}} = & \mathbf{u}_f^{(i,j,k)} \Delta\xi_p^- \Delta\eta_p^- \Delta\zeta_p^- + \mathbf{u}_f^{(i+1,j,k)} \Delta\xi_p^+ \Delta\eta_p^- \Delta\zeta_p^- + \mathbf{u}_f^{(i,j+1,k)} \Delta\xi_p^- \Delta\eta_p^+ \Delta\zeta_p^- \\ & + \mathbf{u}_f^{(i,j,k+1)} \Delta\xi_p^- \Delta\eta_p^+ \Delta\zeta_p^+ + \mathbf{u}_f^{(i+1,j+1,k)} \Delta\xi_p^+ \Delta\eta_p^+ \Delta\zeta_p^- + \mathbf{u}_f^{(i+1,j,k+1)} \Delta\xi_p^+ \Delta\eta_p^- \Delta\zeta_p^+ \\ & + \mathbf{u}_f^{(i,j+1,k+1)} \Delta\xi_p^- \Delta\eta_p^+ \Delta\zeta_p^+ + \mathbf{u}_f^{(i+1,j+1,k+1)} \Delta\xi_p^+ \Delta\eta_p^+ \Delta\zeta_p^+, \end{aligned}\quad (11)$$

where  $\Delta\xi_p^+$ ,  $\Delta\eta_p^+$  and  $\Delta\zeta_p^+$  define the distances of the particle from the node  $(i, j, k)$ . Note that  $\Delta\xi_p^- = 1 - \Delta\xi_p^+$ ,  $\Delta\eta_p^- = 1 - \Delta\eta_p^+$ , and  $\Delta\zeta_p^- = 1 - \Delta\zeta_p^+$ .

Based on the numerical procedure described above, the particle velocity  $\mathbf{u}_p$  can be determined within each time step of the flow prediction of the continuous phase. However, in order to know the actual location of the particle required amongst others for the interpolation formula (11), numerical integration of Eq. (10) is required. Of course, the natural way is to carry out this integration in the physical space, too. Procedures relying on this integration are called *p-space* methods. For a Cartesian (equidistant) grid, this leads to an efficient algorithm because after each integration step the new location of the particle in terms of the indices of the corresponding computational cell can easily be determined taking the explicit relation between the coordinates ( $x, y, z$ ) and the indices  $(i, j, k)$  into account. Contrarily, on a curvilinear body-fitted grid, this advantage is lost completely. That means after each integration step the new particle position with respect to the computational cell has to be determined anew by time-consuming search algorithms (Schäfer & Breuer, 2002). The situation even becomes worse if the grid is separated into different blocks which may be located on different processors during parallel execution.

### 2.2.4. Second numerical integration

In order to enable efficient tracking of millions of particles on a block-structured curvilinear grid, integration of Eq. (10) in the present study is done in *c-space* rather than in *p-space*. In *c-space* schemes, the particle traces are integrated in a coordinate system, in which the curvilinear physical space grid is orthonormal. Point location within the *c-space* grid is as trivial as for a Cartesian grid, since there is an explicit relationship between the *c-space* coordinates of a particle location and the grid cell containing it (Schäfer & Breuer, 2002). Owing to this well-defined coordinate transformation, the *c-space* method has the advantage that no search of the particle's new position is required as for algorithms working in *p-space*. Here, global and local search algorithms such as stencil walk, Newton–Raphson iterative method or tetrahedral walk typically spent the majority of CPU time. With respect to the application of high-performance computers, it is highly beneficial that *c-space* methods do not require such CPU time-killing search algorithms which are moreover difficult to parallelize and vectorize. In Schäfer and Breuer (2002), it was demonstrated that the algorithmic efforts and memory resources required for the vectorization of *p-space* schemes are considerably higher than for *c-space* schemes, depending on the grid and the integration time step that leads to a difference in the CPU time required per time step between *p-space* and *c-space* schemes of up to one order of magnitude.

The transformation of Eq. (10) to the *c-space* leads to

$$\frac{d\xi_p}{dt} = \xi_x u_p + \xi_y v_p + \xi_z w_p = U_p,$$

$$\frac{d\eta_p}{dt} = \eta_x u_p + \eta_y v_p + \eta_z w_p = V_p,$$

$$\frac{d\zeta_p}{dt} = \zeta_x u_p + \zeta_y v_p + \zeta_z w_p = W_p,$$

where the abbreviation  $\partial\xi/\partial x = \xi_x$  and so on is used.  $\mathbf{U}_p = (U_p, V_p, W_p)$  denote the contravariant velocity of the particle which is determined by interpolating the precomputed metric coefficients  $\xi_x, \xi_y, \xi_z, \eta_x, \dots$  of the flow solver to the location of the particle using the same scheme as in Eq. (11). The corresponding particle velocity  $\mathbf{u}_p = (u_p, v_p, w_p)$  is known from the integration of Eq. (7), and hence does not have to be interpolated.

Schäfer and Breuer (2002) compared three different *c*-space tracking schemes (CG, CZ, and CZ+), however, for massless particles, where the right-hand side of Eq. (10) has to be replaced by the fluid velocity. Consequently, for tracking these massless particles the fluid velocity had to be interpolated to the particle location. The highest accuracy and efficiency was found for the so-called CZ+ scheme where the *p*-space instead of the *c*-space velocity was interpolated and the metric terms were computed at the query position. Since in the present algorithm the velocity does not have to be interpolated at all and the metric coefficients are solely predicted at the particle location, the beneficial properties of CZ+ are assigned to the current scheme for particles with inertia.

To determine the new position in *c*-space given by  $(\xi_p, \eta_p, \zeta_p)$ , Eq. (12) is integrated numerically by the same fourth-order Runge–Kutta scheme as used for the first integration step. A back-transformation of the *c*-space coordinates of the particles to *p*-space is not required during the entire algorithm. Solely for visualization purposes such a back-transformation using a trilinear interpolation is carried out to enable the representation in physical coordinates  $(x_p, y_p, z_p)$ .

### 2.2.5. Particle handling and deposition

Based on the new location given in *c*-space coordinates, it can be easily checked whether a particle has left the entire integration domain or the current block of the multi-block arrangement. In the former case, the particle is lost and may be injected again at the source (if desired); in the latter case, the particle with all properties is turned over to the processor which deals with the flow field and particles of the neighboring block. For that purpose, the particle module can rely on the data structure and data exchange routines of the flow solver. On the new block the particle tracking is continued within the next time step of the flow solver.

The last alternative how the number of active particles within a block may change is particle deposition. In a general case, the bounce back of particles which hit the wall is an important mechanism. In the present application, however, it is assumed that the surface of the idealized mouth–throat region (bend) is wet and that the particles adhere to the wetted surface upon contact, i.e.,  $r_p \geq \Delta n_p$ , where  $r_p$  denotes the radius of the particle and  $\Delta n_p$  is the normal distance of the particle center to the surface, respectively. Hence, particle bounce from the bend is not considered to be a problem. Presently, the condition for deposition is even further simplified by assuming that a particle has deposited if its centroid is closer to a wall than the center of the first control volume. This condition is much easier to prove in *c*-space than the previous one and is already sufficiently accurate as will be seen below.

### 2.2.6. High-performance computing aspects

As mentioned above, in order to track a huge number of particles, it is important to work with efficient algorithms which are applicable on high-performance computers typically required for LES. The present scheme is highly efficient due to the following issues:

- No CPU time-consuming search algorithm is needed in the present *c*-space scheme.
- The particle properties are stored in linear arrays which allows vectorization of all loops in the particle routines over the total number of particles on the processor. If the number of particles is reasonably large (e.g., > 256) the loops are efficiently carried out on the vector unit. This pipelining concept also leads to strong performance gains on superscalar RISC processors as used for example in the Hitachi SR 8000-F1.
- Even if particles are leaving the present domain or deposit, the linear arrays are kept filled by reordering the particles after each time step. This guarantees optimal performance.
- The multi-block exchange between blocks for the particle data completely relies on the same arrangement as used for the continuous phase. The data transfer itself is based on MPI.
- Parallelization of the particle routines (and also of the flow solver) is achieved by domain decomposition, i.e., each processor deals with the particles of its own block. A minor disadvantage of this procedure is the fact that no load balancing of the particle tracking is possible, since the distribution of particles is not known in advance. However, since the tracking is so efficient that the predominant part of the CPU time is still spent for the continuous phase,

this imbalance observed for the particle routines does not preponderate for the overall load balancing of the entire code.

### 3. Description of the test case

#### 3.1. Flow and particle parameters

First the combined Eulerian–Lagrangian method was extensively tested based on turbulent particle-laden flows within plane channels and pipes. Here, the dispersion and deposition of particles were investigated for a variety of different cases, e.g., flow Reynolds number, particle diameter, initial conditions (Baytekin, 2004).

As a second step towards the accurate prediction of aerosol drug delivery into the lungs, simulations for the 90° bend flow experiment of Pui et al. (1987) were carried out and the deposition of monodisperse particles was studied in detail. Pui et al. set up this experiment to understand the various particle loss mechanisms, especially the inertial deposition of aerosols in bends. A vibrating orifice generator was used to produce monodisperse test aerosols. A sensitive fluorimetric analysis technique was applied to determine the deposition pattern and deposition efficiency defined as the fraction of particles deposited in the bend to the total number of particles released:

$$\eta = \frac{N_{\text{deposited}}}{N_{\text{total}}}. \quad (12)$$

Particle deposition in bends depends on five dimensionless parameters (Cheng & Wang, 1981; Pui et al., 1987):

- Flow Reynolds number:  $Re_D = U_m D / v_f$ .
- Particle Reynolds number:  $Re_p^* = U_m d_p / v_f$ .
- Curvature ratio:  $R_0 = R_b / (D/2)$ .
- Interception parameter:  $Ic = d_p / D$ .
- Stokes number:  $St = C \rho_p d_p^2 U_m / (18 \mu_f D / 2)$ .

Here,  $U_m$  denotes the mean axial fluid velocity,  $D$  and  $d_p$  the diameters of the bend and the particles,  $R_b$  the axial radius of curvature of the bend, and  $C$  the Cunningham slip correction factor, respectively. Note that the particle Reynolds number is defined differently than in Eq. (8).

The interception parameter  $Ic$  can be neglected since the particle diameter is typically several orders of magnitude less than the tube diameter. If the particle motion is in the Stokesian regime ( $Re_p \leq 1$ ) and the curvature ratio is in the range  $5 \leq R_0 \leq 30$ , the deposition is independent of  $Re_p$  and  $R_0$  (Pui et al., 1987), at least in the turbulent regime. Hence, as the most important parameters, the Stokes number of the particle and the flow Reynolds number remain. Based on Pui et al. (1987) experiments in the present investigation, the flow Reynolds number was set to  $Re_D = 10,000$  and the curvature ratio of the bend was chosen as  $R_0 = 5.6$ . The Stokes number was varied from  $St = 0.001$  to  $1.5$  which covers a wider range than in the measurements. Oleic acid aerosols ( $\rho_p = 895 \text{ kg/m}^3$ ) was used in the experiments carried out with air. Hence, the density ratio required in Eq. (7) is  $\rho_p / \rho_f = 755$ . In total, 250,000 particles randomly distributed over the cross-section (see Section 4.2.2) near the inlet were released within a short (dimensionless) time period of  $\Delta T = 3$  which is normalized by the mean axial velocity  $U_m$  and the radius of the bend  $D/2$ .

The entire geometry is shown in Fig. 1. A horizontal inlet section of length  $D$  is added to the 90° bend. Furthermore, at the outlet the bend is extended by a straight pipe with a length of  $2D$ . These measures guarantee that the inflow and outflow conditions described in the next section do not disturb the flow in the bend itself.

#### 3.2. Boundary conditions

To generate appropriate inflow boundary conditions for the turbulent flow within the bend, which are suited for an LES prediction is not a trivial task since instantaneous velocities for all three velocity components are required. In order to circumvent the generation of artificial inflow data which often only partially satisfy all physical requirements, a separate LES prediction of a pipe with the same cross-section, flow Reynolds number and time step size was carried out. The instantaneous data of one cross-section of this pipe simulation were stored and used as inflow conditions at

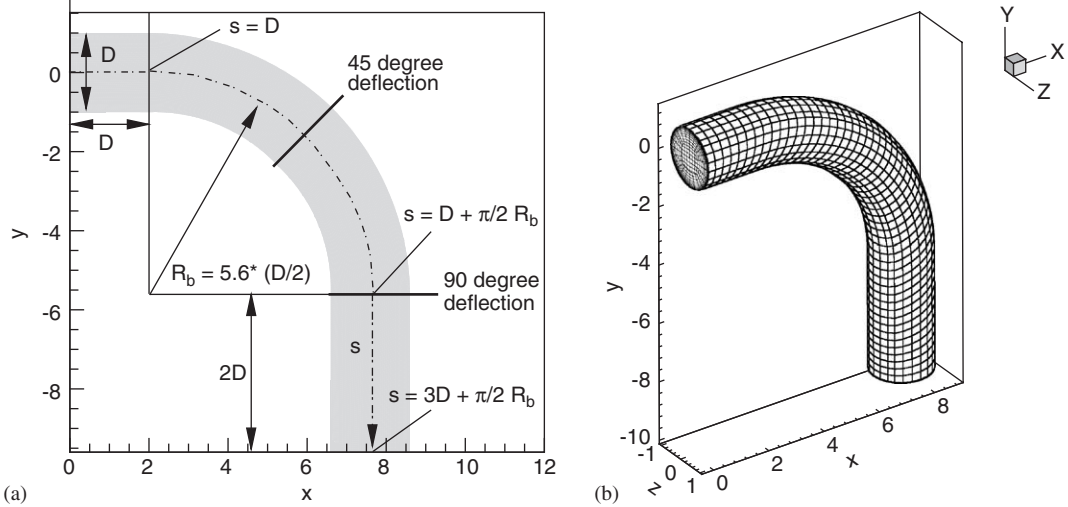


Fig. 1. (a) 2D sketch of the geometric parameters of the bend; (b) 3D surface grid of the bend (only each fifth grid line is displayed).

the inlet of the pipe mounted in front of the bend. That coincides optimally with the experimental set-up where a fully developed flow profile was obtained prior to the bend.

At the outlet of the elongated bend (see Fig. 1) a convective boundary condition was applied which guarantees that all vortical structures can leave the integration domain without significant disturbances or reflections into the inner region (Breuer, 1998, 2002). Finally, at the wall the no-slip boundary condition was used since the grid resolution in the vicinity of the wall is sufficient to resolve the viscous sublayer. The cell center of the wall nearest control volume is located at about  $y^+ = 0.35$ .

### 3.3. Grid

The grid used for the simulations has an O-type structure consisting of five blocks visible in the circular cross-section. In the middle of the cross-section, a nearly rectangular block is generated. The outer region is subdivided into four equal sections which have a nearly polar structure. Compared to a polar grid which is totally orthogonal but has a strong singularity in the center, the present block-structured O-type arrangement avoids this singularity. It is well known that such grid singularities strongly deteriorate the stability and convergence of the solution method as well as the quality of the solution.

The cross-section is discretized with about 8900 grid points which are clustered in the vicinity of the wall based on geometrical series with a stretching factor of 1.05. In streamwise direction, 257 grid points are used which results in about  $2.28 \times 10^6$  grid points in total. Based on previous results for a turbulent plane channel flow (Breuer, 2002) and a turbulent pipe flow (Baytekin, 2004) which used exactly the same cross-sectional grid, the resolution is found to be sufficient to resolve all relevant scales at the moderate Reynolds number considered in the present study.

## 4. Results

### 4.1. Continuous flow field

Regarding the dimensionless parameters mentioned in Section 3.1 the continuous flow field depends on the flow Reynolds number  $Re_D$  and the curvature ratio  $R_0$ . For curvature ratios larger than five, both parameters combined to the Dean number  $De = Re_D/\sqrt{R_0}$  play the role of the Reynolds number for the flow in curved pipes. In the literature, three Dean number ranges are distinguished. At small ( $De \leq 17$ ) and intermediate ( $17 \leq De \leq 370$ ) Dean numbers, a pair of counterrotating helical vortices are formed inside the bend owing to the centrifugally induced pressure gradient. That drives the slower moving fluid near the wall inward, while the faster moving fluid in the core is swept outward

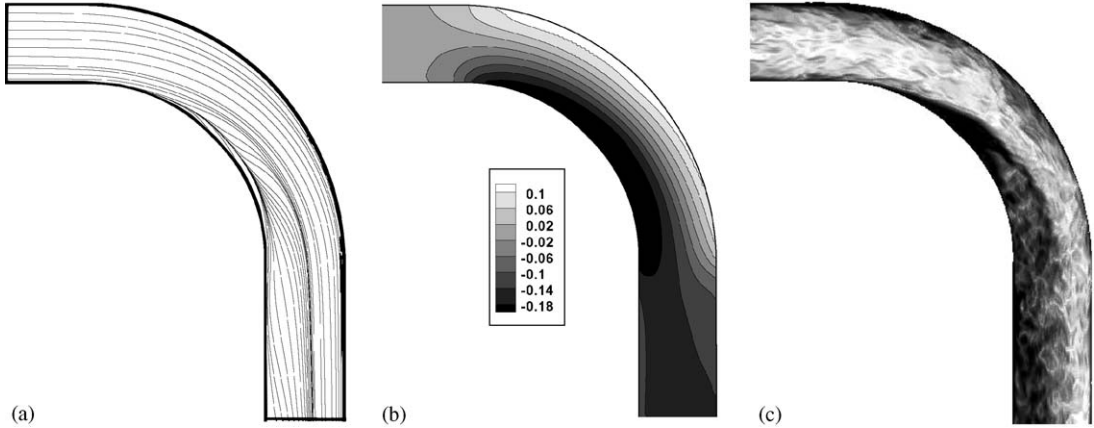


Fig. 2. Turbulent flow in the midplane of the bend at  $Re_D = 10,000$  and  $De = 4225$ : (a) streamlines of the time-averaged flow; (b) pressure distribution of the time-averaged flow; (c) distribution of the velocity magnitude of the instantaneous flow.

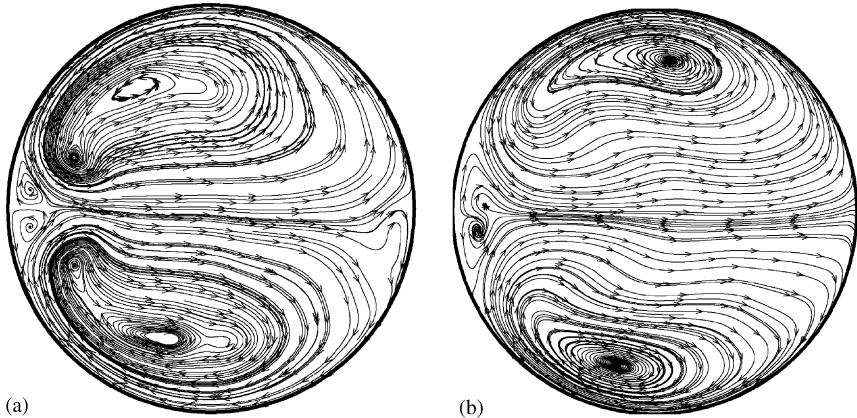


Fig. 3. Streamlines of the time-averaged turbulent flow ( $Re_D = 10,000$  and  $De = 4225$ ) at two cross-sections: (a)  $45^\circ$  deflection and (b)  $90^\circ$  deflection; see Fig. 1 for the definition of the deflection angle.

(Pui et al., 1987) leading to the development of a secondary boundary layer generated by the secondary flow. With increasing  $De$  number the maximum axial velocity moves closer to the outer bend. For large Dean numbers ( $De > 370$ ), i.e., larger centrifugal forces, the secondary boundary layer at the outer bend gets thinner, while near the inner bend the secondary boundary layer is thickening which finally leads to flow separation.

Figs. 2(a) and (b) display the streamlines and pressure distribution in the midplane ( $z = 0$ ) of the bend for the time-averaged flow at  $Re_D = 10,000$  belonging to the large Dean number range ( $De = 4225$ ). As expected, the pressure is low (dark gray) at the inner radius and high (white) at the outer radius. The streamlines in this plane provide an indication to the secondary flow in the bend. This phenomenon can be seen more clearly in cross-sections depicted in Fig. 3 for a deflection angle of  $45^\circ$  and  $90^\circ$ , respectively. Owing to a too short time-averaging period, the flow field is not fully symmetric to the  $z$ -plane. Nevertheless, the main secondary flow structure and its development in axial direction is obvious. That drives the fast moving fluid in the core outward while due to mass conservation the slower moving fluid near the wall is flowing inwards. With increasing deflection, the center of these secondary vortices moves from the inner radius (left) towards the outer radius (right). Owing to the separation process of the secondary boundary layer described above for large  $De$  numbers, an additional secondary flow structure consisting of a pair of counterrotating small vortices is visible at the inner radius. These different phenomena emphasize the complexity of the time-averaged 3D flow. The instantaneous flow field used to track the particles in the bend is even more complex. In Fig. 2(c), the

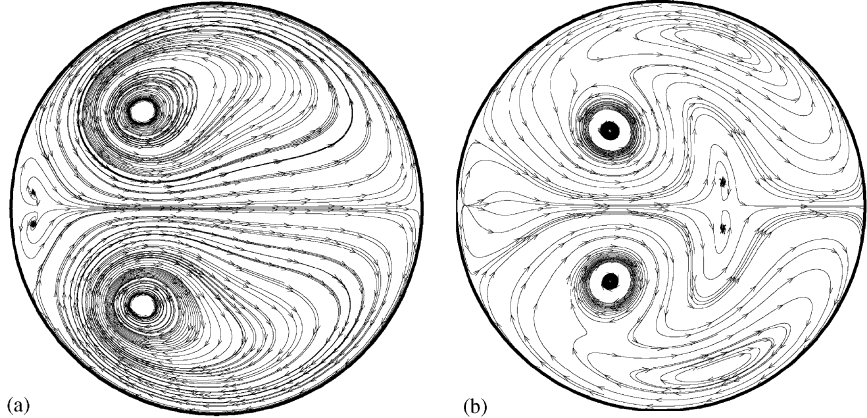


Fig. 4. Streamlines of the steady laminar flow ( $Re_D = 1000$  and  $De = 422.5$ ) at the cross-sections (a) 45° deflection and (b) 90° deflection.

flow in the midplane of the bend is visualized by the magnitude of the velocity at a randomly chosen instant. Turbulent structures appearing in the flow are clearly visible.

For comparison, Fig. 4 displays the same cross-sections for the laminar flow case at  $Re_D = 1000$  and  $De = 422.5$ , which is within the large Dean number range too, and thus the flow is dominated by centrifugal forces. In contrast to the previous case, the flow is steady and laminar. Nevertheless, at a deflection angle of 45°, the flow shows similar secondary flow structures as observed in the turbulent case with ten times larger  $Re_D$  and  $De$  numbers. A pair of main secondary vortices plus a pair of smaller and weaker counterrotating vortices near the inner radius are visible. Quantitatively, of course, large deviations in the position and strength of the secondary flow structures are evident leading to strong differences in the deposition efficiency (see Section 4.2). Interestingly, four pairs of vortices (eight-vortex system) are visible at a deflection angle of 90° with two strong and two weak pairs. This observation is consistent with the literature. It was found that it is attributed to a bifurcation phenomenon whereby a multiple-vortex secondary flow may occur (Jayanti & Hewitt, 1992; Nandakumar & Masliyah, 1982). For example, Yang and Keller (1986) also obtained multiple-vortex solutions including an eight-vortex system in a tube of circular cross-section.

#### 4.2. Particulate phase

##### 4.2.1. Laminar case at $Re_D = 1000$

In order to verify and validate the particle tracking algorithm for a block-structured curvilinear grid working in  $c$ -space, the first case considered for the bend flow is within the steady laminar regime at  $Re_D = 1000$ . In order to speed up the predictions in this case, the control volume approach by Tsai and Pui (1988, 1990) is applied to determine the particle deposition efficiency as follows:

$$\eta = \frac{\sum_{i\text{th C.V.}} \text{deposition}(u_i N_i A_i)}{\sum_{\text{all C.V.s}} (u_i N_i A_i)}, \quad (13)$$

where  $u_i$ ,  $N_i$  and  $A_i$  are the axial flow velocity, the particle concentration, and the area of the  $i$ th control volume at the inlet. The numerator represents the sum of the number of depositing particles passing through the  $i$ th control volume.  $N_i$  particles are randomly distributed over each control volume face at the inlet and tracked through the flow field until they exited the bend or deposited at the wall. The accuracy of this method can be estimated (Tsai & Pui, 1988) and was found to be sufficient. Here,  $N_i$  was varied between 1 and 10 leading to a maximum of about 76,000 particles which were used for the determination of the deposition efficiency in the laminar case.<sup>1</sup>

For different particle diameters characterized by the Stokes number  $St$ , the deposition efficiency  $\eta$  was determined. Fig. 5 depicts the predicted results. For comparison with the present predictions, the experimental data of Pui et al. (1987) and the numerical results by Cheng and Wang (1981) as well as Tsai and Pui (1990) are available and included

<sup>1</sup> For this case, no gravitational acceleration was taken into account.

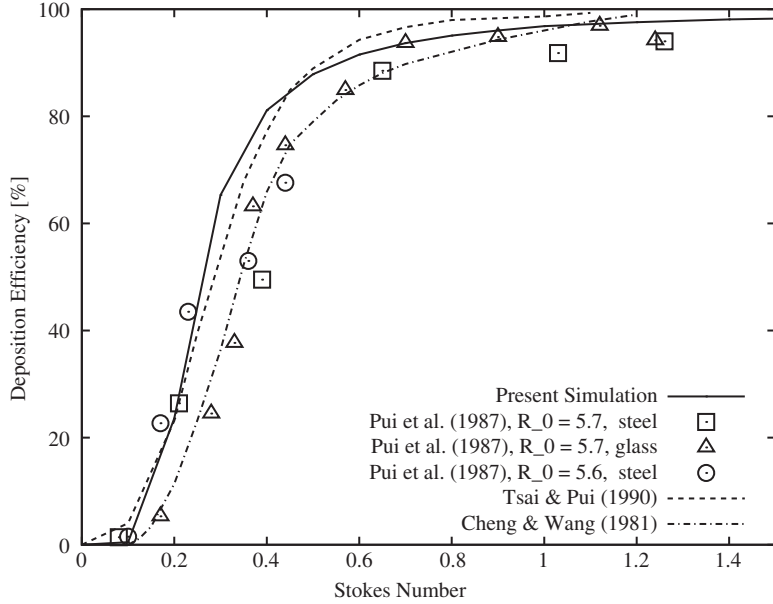


Fig. 5. Deposition efficiency  $\eta$  of particles for the laminar bend flow at  $Re_D = 1000$ .

in Fig. 5. Pui et al. (1987) carried out three different set of experiments at this Reynolds number, two with stainless steel tubes and one with a glass tube. The curvature ratio  $R_0$  of the tubes was varying between 5.6 and 5.7. The different experimental data are slightly scattered especially for low Stokes numbers which is attributed to experimental errors in the wiping procedure used to determine the deposition efficiencies. The curve predicted by the present approach is within the range of the experimental uncertainty. Cheng and Wang (1981) calculated the trajectories of particles in a 90° bend using a fully developed laminar flow. This analytically described flow field, consisting of a core region and a laminar boundary layer, was proposed and experimentally verified by Mori and Nakayama (1965). Since the Mori–Nakayama solution was derived for flows at relatively large Reynolds numbers in the laminar regime, from the two cases investigated by Cheng and Wang (1981) at a curvature ratio  $R_0 = 8.0$  only the higher-Re case at  $Re_D = 1000$  is useful here for comparison. These data show slightly lower deposition efficiencies than the present predictions. However, Tsai and Pui (1990) investigated the influence of the inlet velocity profile used for the computation of the laminar flow. They found a strong influence on the deposition efficiency. In the case of a parabolic velocity profile as used in the present predictions, the deposition efficiency is always much higher than that of a non-developed uniform profile. The reason are the higher centrifugal forces generated for the parabolic profile in comparison with the uniform case. Therefore, only the results predicted by Tsai and Pui (1990) for a parabolic inlet profile are included in Fig. 5. These predictions are in close agreement with the present ones.

As expected, large particles of high inertia are unable to flow the continuous flow and thus collide with the outer wall of the curved bend. This phenomenon is visible in Figs. 6 and 7 which depict the deposition patterns for two different Stokes numbers. At  $St = 1.0$ , most particles deposit at the outer wall which agrees with experimental observations by Pui et al. (1987). High values of the deposition efficiency  $\eta$  are found in that case. On the other hand, small particles with low inertia follow the continuous flow closely and mostly penetrate through the bend yielding low values of  $\eta$ . Owing to the secondary flow structures described in Section 4.1, the lighter particles do not deposit at the outer wall of the bend but at the side walls and the inner walls as visible in Figs. 6(a) and 7(a) for  $St = 0.2$  which is also in agreement with the observations by Pui et al. (1987). To sum up, the different deposition patterns are a consequence of the particle inertia and secondary flow in the bend.

For fixed flow conditions ( $Re_D$ ,  $R_0$ ), the question whether a particle penetrates through the bend or deposits at the wall depends solely on the initial particle position and the Stokes number. Hence, two interesting questions can be answered.

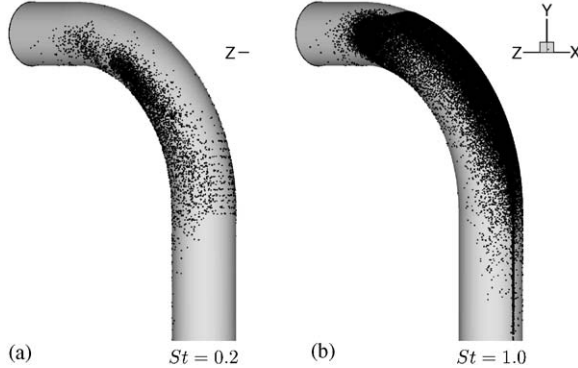


Fig. 6. Deposition patterns for the steady laminar flow ( $Re_D = 1000$  and  $De = 422.5$ ) at two different Stokes numbers: (a)  $St = 0.2$  and (b)  $St = 1.0$ ; view showing the outer bend.

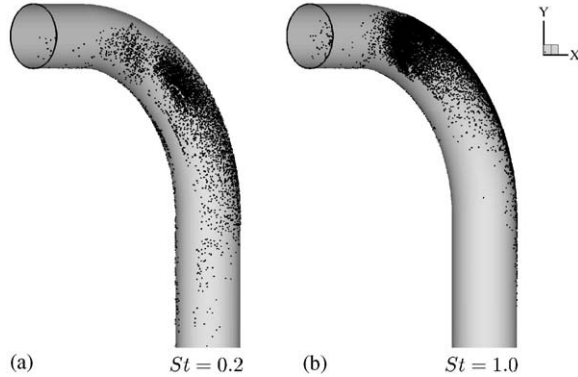


Fig. 7. Deposition patterns for the steady laminar flow ( $Re_D = 1000$  and  $De = 422.5$ ) at two different Stokes numbers: (a)  $St = 0.2$  and (b)  $St = 1.0$ ; view showing the inner bend.

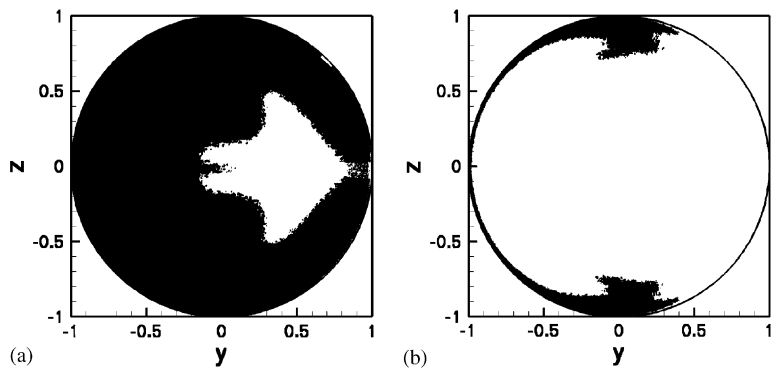


Fig. 8. Deposition regions (white) and penetration regions (black) at the inlet section for the steady laminar flow ( $Re_D = 1000$  and  $De = 422.5$ ) at two different Stokes numbers: (a)  $St = 0.2$  and (b)  $St = 1.0$ .

First, for a fixed  $St$  number in the range  $0.1 \leq St \leq 1.5$ , the initial positions at the inlet cross-section leading to deposition can be determined. That is shown for two different Stokes numbers in Fig. 8. The white areas display the starting positions of those particles which will deposit during their flight through the bend. At  $St = 0.2$ , this region is located around the symmetry line in the upper part of the cross-section, whereas at  $St = 1.0$  it covers nearly the entire

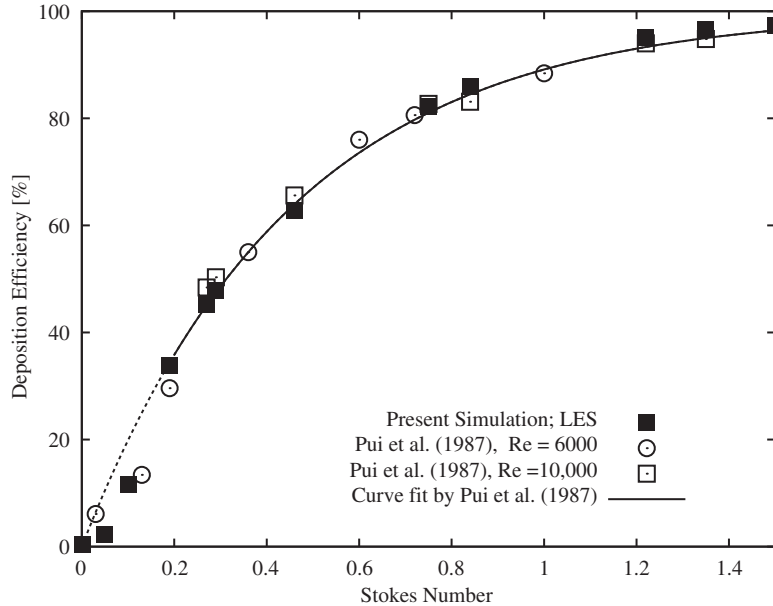


Fig. 9. Deposition efficiency  $\eta$  of particles for the turbulent bend flow at  $Re_D = 10,000$ .

cross-section. In that case, only a small region next to the side walls of the bend remains from which injected particles penetrate through the bend.

Second, for a given initial distribution at the inlet, the impact efficiency depending on  $St$  can be evaluated as shown in Fig. 5. Below a lower limit of  $St \approx 0.1$ , all particles penetrate through the bend. Above an upper limit of  $St \approx 1.5$ , nearly no particle can follow the continuous phase and hits the outer bend wall leading to deposition efficiencies which asymptotically approach 100%.

#### 4.2.2. Turbulent case at $Re_D = 10,000$

After the extensive validation of the methodology based on the laminar flow, the more challenging case of a turbulent flow at  $Re_D = 10,000$  is considered using LES. Since the flow is unsteady, the control volume approach given by Eq. (13) cannot be applied in this case and Eq. (12) is used instead. For that purpose, 250,000 particles randomly distributed over the cross-section near the inlet were released and tracked through the flow field until they exited the bend or deposited at the wall. To ensure particle statistics of high quality, the number of released particle was set to this large value. Based on theoretical considerations, it can be estimated that one particle source per control volume at the inlet releasing particles at 10 statistically independent instants should be sufficient to guarantee a reasonable accuracy within a few percent. Therefore, about a fifth part of the presently released particles are assumed to be sufficient to reach this error bound.

For different particle diameters characterized by the Stokes number, the deposition efficiency was determined. Fig. 9 depicts the predicted results in comparison to the measurements of Pui et al. (1987) at two different flow Reynolds numbers, i.e.,  $Re_D = 6000$  and 10,000. The experimental data of both Reynolds numbers are included, since in the range considered the deposition efficiency was found to be independent on  $Re_D$  (Pui et al., 1987). Furthermore, a curve fitted through the experimental data is added which describes the deposition efficiency as a function of the Stokes number:

$$\eta = 1 - \underbrace{10^{-0.963St}}_P. \quad (14)$$

Here,  $P$  denotes the penetration ratio. The deposition efficiencies predicted by LES with the fast tracking algorithm described above are in very good agreement with the experimental data over the entire Stokes number range considered. For large Stokes numbers, the deposition efficiency asymptotically approaches 100% (e.g.,  $\eta = 97.4\%$  at  $St = 1.5$ ). For small Stokes numbers,  $\eta$  goes to zero as expected. However, it is interesting to investigate in detail the behavior

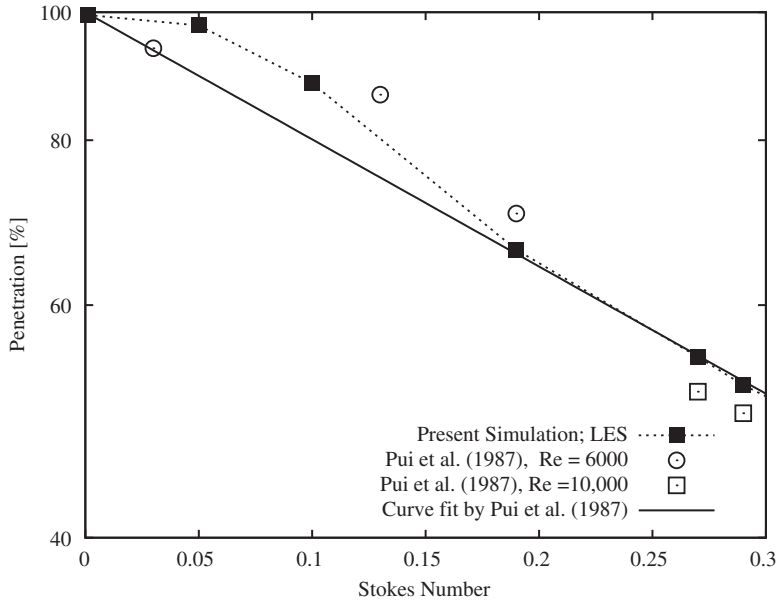


Fig. 10. Penetration ratio  $P$  of particles for the turbulent bend flow at  $Re_D = 10,000$  at low Stokes numbers.

in the limit  $St \rightarrow 0$ . At  $St = 0.1$ , the deposition efficiency is still high, i.e.  $\eta = 11.64\%$ . When reducing the Stokes number by a factor of 2,  $\eta$  decreases to a level of about 2.3% which is much less than the value of about 10.5% provided by relation (14). This behavior in the vicinity of vanishing Stokes numbers is depicted in Fig. 10 in terms of the penetration ratio  $P = 1 - \eta$  versus  $St$  in a semilog scale. Based on the present predictions, it is questionable whether relation (14) holds for low Stokes numbers.<sup>2</sup> Obviously, the results deviate from the theoretically given straight line in the semilog scale. Similar to the findings in the laminar regime, the deposition efficiency versus the Stokes number shows an inflection point and approaches zero for finite Stokes numbers. Contrarily, the exponential relation by Pui et al. (1987)  $\eta$  approaches zero for  $St = 0$ .

In order to study the deposition behavior, patterns of the deposited particles are shown in Fig. 11 for six different Stokes numbers. The view of the observer is directed towards the outer bend. Additionally, Fig. 12 displays the same results from a viewpoint which allows to see the inner bend. At low Stokes numbers, e.g.  $St = 0.05$  and  $0.10$ , the deposition ratio is low. The small particles with low inertia are able to follow the continuous flow closely and mostly leave the bend through the exit. Owing to the secondary flow structure found in the bend a minority of the particles deposit at the side wall and partially also at the inner bend. This observation is similar to the laminar case shown in Figs. 6(a) and 7(a). Furthermore, it agrees well with the observations by Pui et al. (1987) made in their experimental set-up using glass tubes.

With increasing size of the particles the inertial forces are increasing, and consequently more and more particles are no longer able to flow the secondary flow in the bend. Hence, they deposit at the outer bend wall owing to centrifugal forces. At the highest Stokes numbers, the deposition ratio at the side walls is reduced again since nearly all particles deposit at the outer bend. This behavior is consistent with the experimental observations by Pui et al. (1987). They reported that for large Stokes numbers, the outer bend was completely covered with a layer of particles. The entire deposition behavior of the particles at different Stokes numbers is summarized in Fig. 13 which shows the distribution of the particle deposition along the perimeter of the bend. All trends discussed above are visible in this diagram.

An interesting feature is visible in Fig. 12. For all Stokes numbers predicted, a stripe at the inner bend remains clean, i.e., no deposition takes place in this region. The reason for this phenomenon is the additional secondary flow structure consisting of a pair of counterrotating small vortices at the inner bend radius. These structures were already visualized in Fig. 3 for the time-averaged flow field. Although the particle motion is determined by the instantaneous flow field,

<sup>2</sup> Therefore, it is displayed in Fig. 9 only by a dashed line for  $St < 0.2$ .

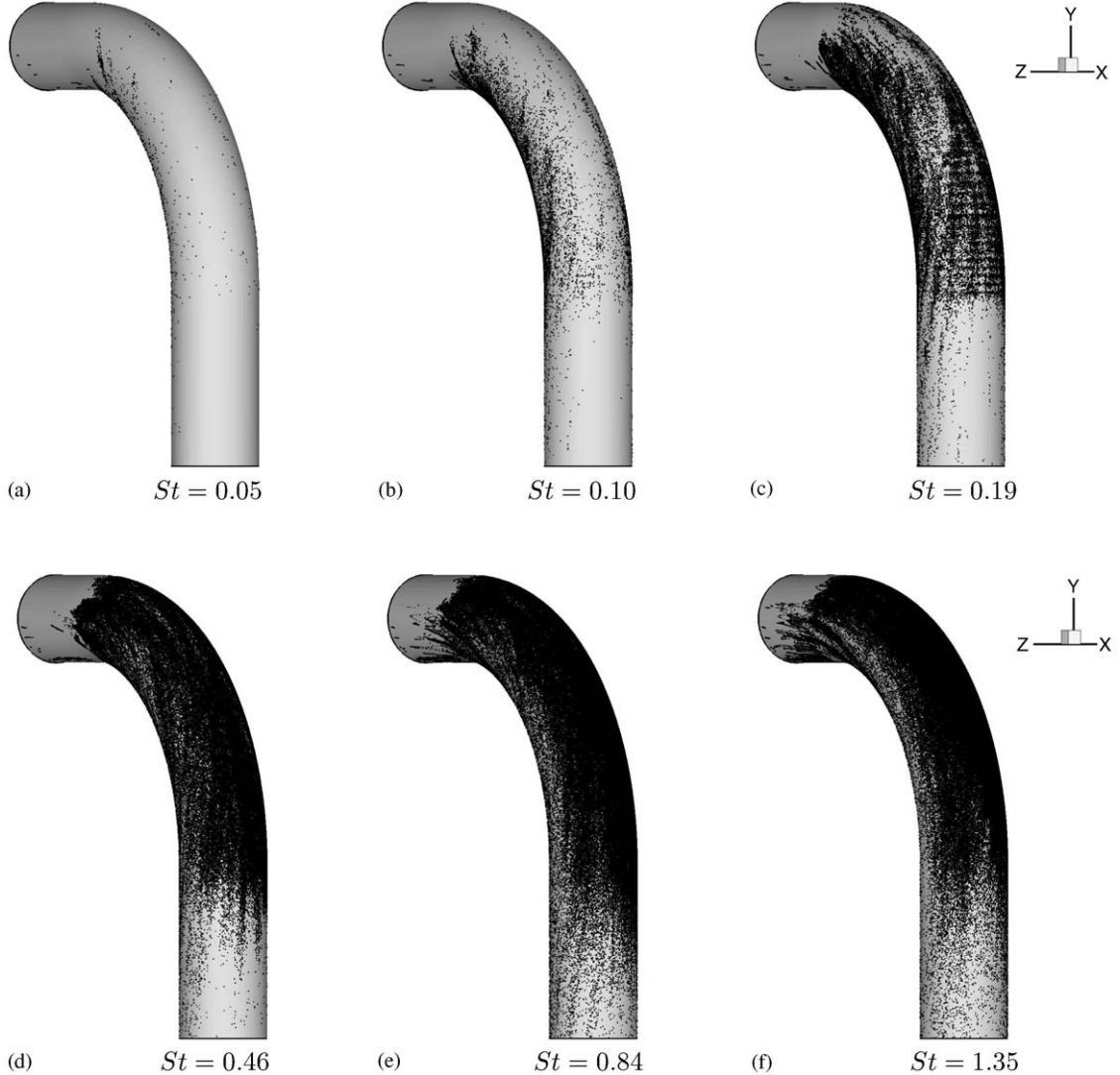


Fig. 11. Deposition patterns for the turbulent flow ( $Re_D = 10,000$  and  $De = 4225$ ) at six different Stokes numbers: (a)  $St = 0.05$ , (b)  $St = 0.10$ , (c)  $St = 0.19$ , (d)  $St = 0.46$ , (e)  $St = 0.84$ , and (f)  $St = 1.35$ ; view showing the outer bend.

in the mean, this pair of counterrotating vortices prevent particles from depositing along a stripe at the inner radius of the bend. This finding is not reported in the study by Pui et al. (1987).

Finally, Fig. 14 depicts the distribution of the particle deposition along the bend axis  $s/(D/2)$ . The definition of  $s$  is given in Fig. 1. Obviously, some particles already deposit in the straight inlet section ( $0 \leq s \leq D$ ) in front of the bend. The number of deposited particles in this region is increasing with the Stokes number. When entering the bend the deposition ratio strongly increases where the gradient observed is coupled to the Stokes number. A peak value is reached in the region of about  $6^\circ$  to  $15^\circ$  bend deflection for Stokes numbers  $St \geq 0.46$ . A second pronounced maximum is found at about  $45^\circ$  bend deflection for  $St = 1.35$ . However, with decreasing Stokes number, this second maximum is decreasing and its location shifted towards about  $80^\circ$ . The reason for this behavior can be explained again by the inertial forces. Lighter particles are following the secondary flow in the bend more closely and hence are transported towards the outlet before deposition takes place whereas heavier particles are depositing much earlier. In the straight outlet pipe past the bend ( $D + \Pi/2 R_b \leq s \leq 3D + \Pi/2 R_b$ ), the deposition ratio strongly drops off for all Stokes numbers as expected.

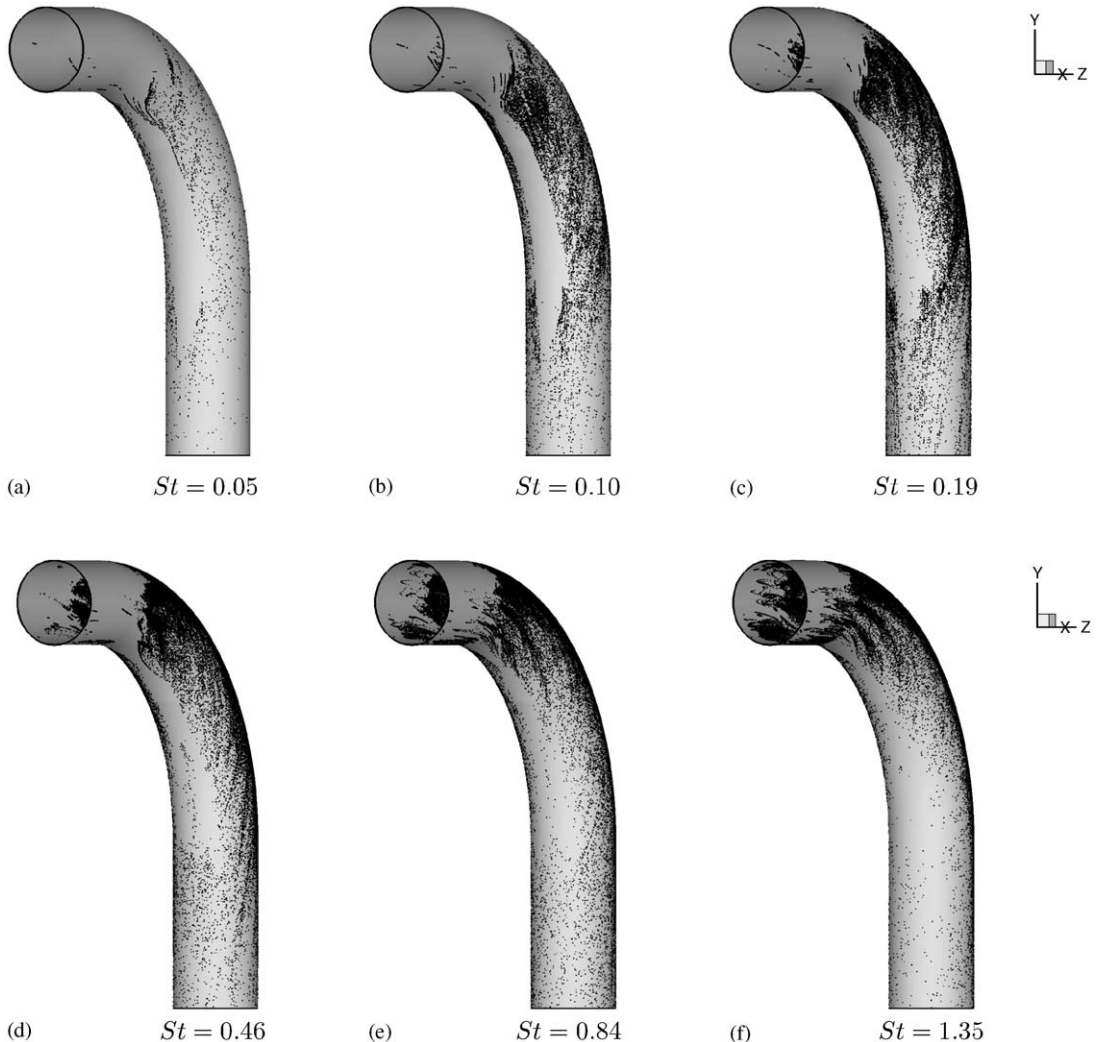


Fig. 12. Deposition patterns for the turbulent flow ( $Re_D = 10,000$  and  $De = 4225$ ) at six different Stokes numbers: (a)  $St = 0.05$ , (b)  $St = 0.10$ , (c)  $St = 0.19$ , (d)  $St = 0.46$ , (e)  $St = 0.84$ , and (f)  $St = 1.35$ ; view showing the inner bend.

## 5. Conclusion

The paper describes an efficient and accurate methodology to predict turbulent particle-laden flows which are of great relevance in many technical as well as medical applications, e.g. the pharmaceutical aerosol deposition in extrathoracic airways. The continuous phase is predicted applying the LES technique on block-structured curvilinear grids. For the particulate phase, the Lagrangian approach is used tracking individual monodisperse particles through the flow field. In order to study the behavior of hundred thousands of particles, a highly efficient tracking algorithm was developed. The key feature of this method is the integration of the governing equation for the particle position in the computational space rather than in the physical space. This procedure completely avoids time-consuming search algorithms, normally required for methods working in the physical domain of a body-fitted block-structured grid. The particulate and the continuous phase predictions exploit the full potential of high-performance computers including vectorization and parallelization using domain decomposition based on MPI.

The methodology was applied to the particle-laden turbulent flow through a  $90^\circ$  bend with tubular cross-section at  $Re_D = 10,000$ . For the purpose of verification and validation, the same configuration was investigated first at

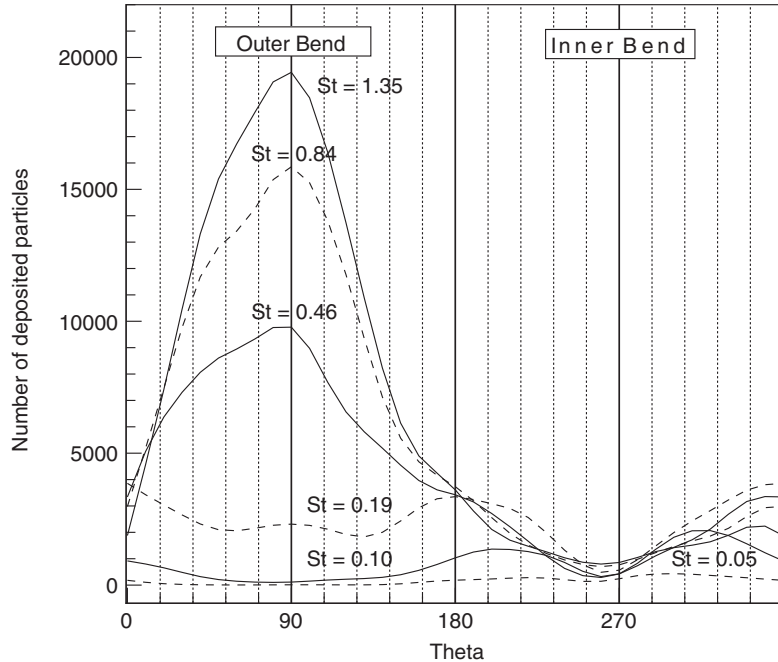


Fig. 13. Distribution of particle deposition along the perimeter of the bend at  $Re_D = 10,000$  and  $De = 4225$  at six different Stokes numbers  $St = 0.05, 0.10, 0.19, 0.46, 0.84$ , and  $1.35$ . (Outer bend radius at  $\Theta = 90^\circ$ .)

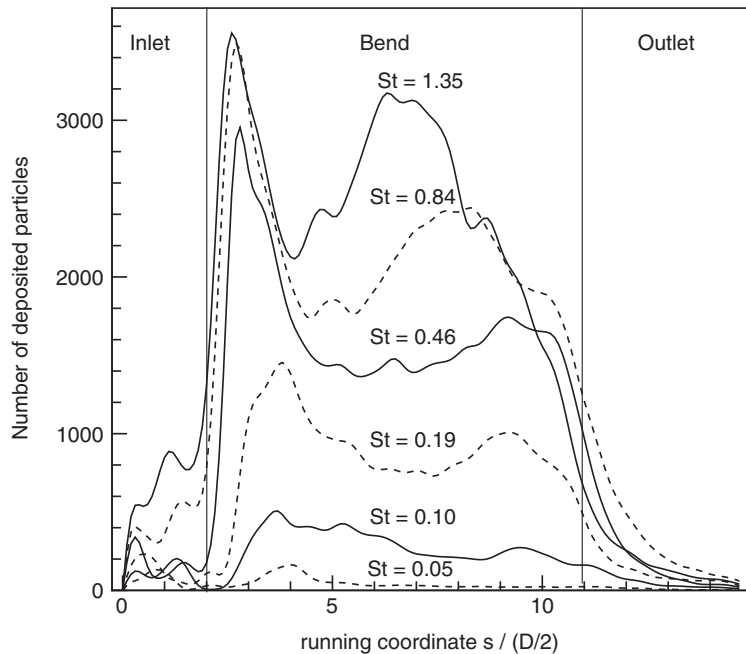


Fig. 14. Distribution of particle deposition along the  $s$ -axis (see Fig. 1 for the definition of  $s$ ) of the bend at  $Re_D = 10,000$  and  $De = 4225$  at six different Stokes numbers  $St = 0.05, 0.10, 0.19, 0.46, 0.84$ , and  $1.35$ .

$Re_D = 1000$  within the laminar regime and good agreement with previous studies was found. For the more challenging case of turbulent flow, the deposition efficiency of particles in the range  $0.001 \leq St \leq 1.5$  was determined and excellent agreement with the measurements by Pui et al. (1987) was found. It is shown that the curve fit (Pui et al., 1987) is not valid for  $St \leq 0.2$ . Instead the distribution  $\eta(St)$  has an inflection point and approaches zero at finite Stokes numbers. Furthermore, the deposition patterns for varying Stokes numbers were studied in detail. Besides the inertial forces acting on the particles, the secondary flow in the bend has the strongest influence on the particles trajectories. At least for low Stokes numbers, the particles can closely follow the continuous flow. Consequently, particles deposit not only at the outer bend but also at the side walls and the inner bend.

An interesting feature detected for the first time is a stripe at the inner bend which remains clean for all Stokes numbers predicted. The reason why no deposition takes place in this region is found in the additional secondary flow structure consisting of a pair of counterrotating small vortices at the inner bend radius which prevents particles to reach this area.

In conclusion, the methodology described in this paper and the corresponding simulations for the turbulent bend flow represent a valuable step towards the prediction of the inhalation process in the entire mouth–throat region which is planned for the near future.

## Acknowledgments

The present work was carried out as a part of the Center of Excellence SFB 603 “*Model-Based Analysis and Visualization of Complex Scenes and Sensor Data*” at the University of Erlangen-Nuremberg. E. A. M. visited Erlangen as a guest researcher supported by SFB 603. Financial support by the “*Deutsche Forschungsgemeinschaft*” is gratefully acknowledged.

## References

- Armenio, V., Piomelli, U., & Fiorotto, V. (1999). Effect of the subgrid scales on particle motion. *Physics of Fluids*, 11(10), 3030–3042.
- Baytekin, H. T. (2004). *Investigations of particle dispersion and deposition for turbulent flows in channels, pipes and bends based on LES predictions*. M.Sc. thesis, Universität Erlangen-Nürnberg.
- Breuer, M. (1998). Large-eddy simulation of the sub-critical flow past a circular cylinder: Numerical and modeling aspects. *International Journal for Numerical Methods in Fluids*, 28, 1281–1302.
- Breuer, M. (2000). A challenging test case for large-eddy simulation: High Reynolds number circular cylinder flow. *International Journal of Heat and Fluid Flow*, 21(5), 648–654.
- Breuer, M. (2002). Direkte Numerische Simulation und Large-Eddy Simulation turbulenter Strömungen auf Hochleistungsrechnern, Habilitationsschrift. Universität Erlangen-Nürnberg, Berichte aus der Strömungstechnik. ISBN: 3-8265-9958-6. Aachen: Shaker Verlag.
- Breuer, M., & Rodi, W. (1996). Large-eddy simulation of complex turbulent flows of practical interest. In E.H. Hirschel (Ed.), *Flow simulation with high-performance computers II. Notes on Numerical Fluid Mechanics*, Vol. 52 (pp. 258–274). Braunschweig: Vieweg.
- Chen, M., & McLaughlin, J. B. (1995). A new correlation for the aerosol deposition rate in vertical ducts. *Journal of Colloid and Interface Science*, 169, 437–455.
- Cheng, Y. S., & Wang, C. S. (1981). Motion of particles in bends of circular pipes. *International Journal of Atmospheric Environment*, 15, 301–306.
- Cheng, Y. S., Zhou, Y., & Chen, B. T. (1999). Particle deposition in a cast of human oral airways. *Aerosol Science and Technology*, 31, 286–300.
- DeHaan, W. H., & Finlay, W. H. (2001). In vitro monodisperse aerosol deposition in a mouth and throat with six different inhalation devices. *Journal of Aerosol Medicine*, 14(3), 361–367.
- Finlay, W. H. (2001). *The mechanism of inhaled pharmaceutical aerosols: An introduction*. London: Academic Press.
- Germano, M., Piomelli, U., Moin, P., & Cabot, W. H. (1991). A dynamic subgrid scale eddy viscosity model. *Physics of Fluids A*, 3(7), 1760–1765.
- Jayanti, S., & Hewitt, G. F. (1992). A numerical study of bifurcation in laminar flow in curved ducts. *International Journal for Numerical Methods in Fluids*, 14, 253–266.
- Lilly, D. K. (1967). The representation of small-scale turbulence in numerical simulation experiments. In H.H. Goldstine (Ed.), *Proceedings of the IBM Scientific Computing Symposium on Environmental Sciences* (pp. 195–210). IBM Forum no. 320-1951.
- Lilly, D. K. (1992). A proposed modification of the Germano subgrid scale closure method. *Physics of Fluids A*, 4(3), 633–635.
- Matida, E. A., Breuer, M., Finlay, W. H., & Lange, C. F. (2004). Large-eddy simulation of aerosol deposition in an idealized mouth with a small inlet. CFD 2004—The Twelfth Annual Conference of the CFD Society of Canada, Ottawa, Ont., Canada, May 9–11.
- Matida, E. A., Finlay, W. H., Lange, C. F., & Grgic, B. (2004). Improved numerical simulation of aerosol deposition in an idealized mouth–throat. *Journal of Aerosol Science*, 35, 1–19.
- McFarland, A. R., Gong, H., Muyshondt, A., Wente, W. B., & Anand, N. K. (1997). Aerosol deposition in bends with turbulent flow. *Environmental Science and Technology*, 31(12), 3371–3377.
- Mori, Y., & Nakayama, W. (1965). Study on forced convective heat transfer in curved pipes: I. Laminar region. *International Journal of Heat and Mass Transfer*, 8, 67–82.

- Nandakumar, K., & Masliyah, J. H. (1982). Bifurcation in steady laminar flow through curved tubes. *Journal of Fluid Mechanics*, 119, 475–490.
- Pui, D. Y. H., Romay-Novas, F., & Liu, B. Y. H. (1987). Experimental study of particle deposition in bends of circular cross-section. *Aerosol Science and Technology*, 7, 301–315.
- Rhie, C. M., & Chow, W. L. (1983). A numerical study of the turbulent flow past an isolated airfoil with trailing edge separation. *AIAA Journal*, 21, 1525–1532.
- Schäfer, F., & Breuer, M. (2002). Comparison of *C*-space and *P*-space particle tracing schemes on high-performance computers: Accuracy and performance. *International Journal for Numerical Methods in Fluids*, 39, 277–299.
- Schiller, L., & Naumann, A. (1933). A drag coefficient correlation. *VDI Zeitschrift*, 77, 318–320.
- Smagorinsky, J. (1963). General circulation experiments with the primitive equations. I. The basic experiment. *Monthly Weather Review*, 91, 99–165.
- Stahlhofen, W., Rudolf, G., & James, A. C. (1989). Intercomparison of experimental regional aerosol deposition data. *Journal of Aerosol Medicine*, 2, 285–308.
- Stapleton, K. W., Guentsch, E., Hoskinson, M. K., & Finlay, W. H. (2000). On the suitability of  $k$ - $\varepsilon$  turbulence modeling for aerosol deposition in the mouth and throat: A comparison with experiment. *Journal of Aerosol Science*, 31(6), 739–749.
- Stone, H. L. (1968). Iterative solution of implicit approximations of multidimensional partial differential equations. *SIAM Journal on Numerical Analysis*, 5, 530–558.
- Tsai, C. J., & Pui, D. Y. H. (1988). *University of Minnesota Supercomputer Institute Report*. UMSI 88/115.
- Tsai, C. J., & Pui, D. Y. H. (1990). Numerical study of particle deposition in bends of a circular cross-section—laminar flow regime. *Aerosol Science and Technology*, 12, 813–831.
- Uijttewaal, W. S. J., & Oliemans, R. V. A. (1996). Particle dispersion and deposition in direct numerical and large-eddy simulations of vertical pipe flows. *Physics of Fluids*, 8(10), 2590–2604.
- Wang, Q., & Squires, K. D. (1996). Large-eddy simulation of particle deposition in a vertical turbulent channel flow. *International Journal of Multiphase Flow*, 22(4), 667–683.
- Wang, Q., Squires, K. D., Chen, M., & McLaughlin, J. B. (1997). On the role of the lift force in turbulence simulations of particle deposition. *International Journal of Multiphase Flow*, 23(4), 749–763.
- Yang, Z., & Keller, H. B. (1986). Multiple laminar flows through curved pipes. *Applied Numerical Analysis*, 2, 257–271.